nature electronics

ARTICLES

https://doi.org/10.1038/s41928-020-0441-9

Check for updates

High tunnelling electroresistance in a ferroelectric van der Waals heterojunction via giant barrier height modulation

Jiangbin Wu[1,8], Hung-Yu Chen[1,8], Ning Yang[2], Jun Cao[3], Xiaodong Yan[1], Fanxin Liu[4], Qibin Sun[5] ✉, Xi Ling[3,6], Jing Guo[2] ✉ and Han Wang[1,7] ✉

Ferroelectric tunnel junctions use a thin ferroelectric layer as a tunnelling barrier, the height of which can be modified by switching its ferroelectric polarization. The junctions can offer low power consumption, non-volatile switching and non-destructive readout, and thus are promising for the development of memory and computing applications. However, achieving a high tunnelling electroresistance (TER) in these devices remains challenging. Typical junctions, such as those based on barium titanate or hafnium dioxide, are limited by their small barrier height modulation of around 0.1 eV. Here, we report a ferroelectric tunnel junction that uses layered copper indium thiophosphate ($CuInP_2S_6$) as the ferroelectric barrier, and graphene and chromium as asymmetric contacts. The ferroelectric field effect in $CuInP_2S_6$ can induce a barrier height modulation of 1 eV in the junction, which results in a TER of above 10^7. This modulation, which is shown using Kelvin probe force microscopy and Raman spectroscopy, is due to the low density of states and small quantum capacitance near the Dirac point of the semi-metallic graphene.

A ferroelectric tunnel junction (FTJ) is a two-terminal vertical heterostructure that can switch between two or more conductance states in a reversible and non-volatile manner[1–5]. In FTJs, an ultra-thin ferroelectric layer is used as the tunnelling barrier and its average barrier height (ABH) can be modified by switching the ferroelectric polarization. The change in the electrical conductance of the junction due to this polarization reversal results in its tunnelling electroresistance (TER)[1,6,7]. There are two main types of ferroelectric material used in existing FTJs: ABO-type perovskites[1,2,4,8,9], such as $BaTiO_3$ (BTO) and $PbZr_{0.2}Ti_{0.8}O_3$, and binary oxides[10,11], such as HfO_2 and $Hf_{0.5}Zr_{0.5}O_2$ (HZO). In FTJs based on ABO-type perovskites, the TER can reach values of around 10^6, although this requires incorporation of an additional semiconducting layer in a complex structure in which barrier height and width are both modulated by the polarization field[12]. The ferroelectric materials also have to be grown on a perovskite-based substrate[1,4,12], which limits compatibility with existing electronics technology. FTJs based on binary oxides have been extensively explored, but have TER values below 100 due to the limitations of the traditional FTJ modulation mechanism and intrinsic material properties[13–16]. Importantly, the TER in both types of FTJ structure is constrained by the relatively small modulation of the tunnelling barrier height, which is typically below 0.1 eV with either metallic or semiconducting contacts[15,17].

Recently, ferroelectric properties have been observed in two-dimensional (2D) van der Waals (vdW) materials such as $CuInP_2S_6$ (CIPS) and α-In_2Se_3 (refs. [18–31]). The transition temperatures of these materials are well above room temperature[18,19,22,23] and the materials are compatible with industrial silicon electronics processes[32–34]. In this Article, we report FTJs based on a 2D vdW heterostructure in which CIPS is used as the ferroelectric tunnelling barrier layer and chromium and monolayer graphene (1LG) are used as asymmetric electrodes. Such FTJs exhibit a giant TER of above 10^7. We attribute this behaviour to a large change of the ABH, which results from the large Fermi level shift in graphene spontaneously induced by the polarization field in the adjacent CIPS. Owing to the low density of states in graphene near its Dirac point and its small quantum capacitance, this Fermi level shift can approach 1 eV.

The vdW FTJ structure and electrical characteristics

Figure 1a presents a schematic diagram of the vdW FTJ (see Supplementary Fig. 1 for the optical image), where the layered CIPS (see Supplementary Fig. 2 for the Raman spectrum)[35,36] is used as the ferroelectric tunnelling barrier layer, and graphene and Cr are used as the asymmetric electrodes. The scanning transmission electron microscopy (STEM) and electron energy loss spectroscopy (EELS) images in Fig. 1b clearly show the material compositions in the Cr/CIPS/graphene layered heterostructure. To characterize the ferroelectric properties in the CIPS material, piezoelectric force microscopy (PFM) and capacitance–voltage (C–V) measurements were performed in the metal–CIPS–metal (Au/CIPS/Cr) structure, as shown in Fig. 1c,d. For the PFM measurements in Fig. 1c, both the amplitude and phase of the piezoelectric response show hysteresis loops, indicating the existence of ferroelectricity. The hysteresis in the C–V characteristics (Fig. 1d) shows the typical butterfly shape with a coercive field of ~0.14 V nm^{-1}, consistent with the PFM

[1]Ming Hsieh Department of Electrical and Computer Engineering, University of Southern California, Los Angeles, CA, USA. [2]Department of Electrical and Computer Engineering, University of Florida, Gainesville, FL, USA. [3]Department of Chemistry, Boston University, Boston, MA, USA. [4]Collaborative Innovation Center for Information Technology in Biological and Medical Physics, and College of Science, Zhejiang University of Technology, Hangzhou, People's Republic of China. [5]University of Science and Technology of China, Hefei, People's Republic of China. [6]Division of Materials Science and Engineering, Boston University, Boston, MA, USA. [7]Mork Family Department of Chemical Engineering and Material Science, University of Southern California, Los Angeles, CA, USA. [8]These authors contributed equally: Jiangbin Wu, Hung-Yu Chen. ✉e-mail: qibinsun@ustc.edu.cn; guoj@ufl.edu; han.wang.4@usc.edu

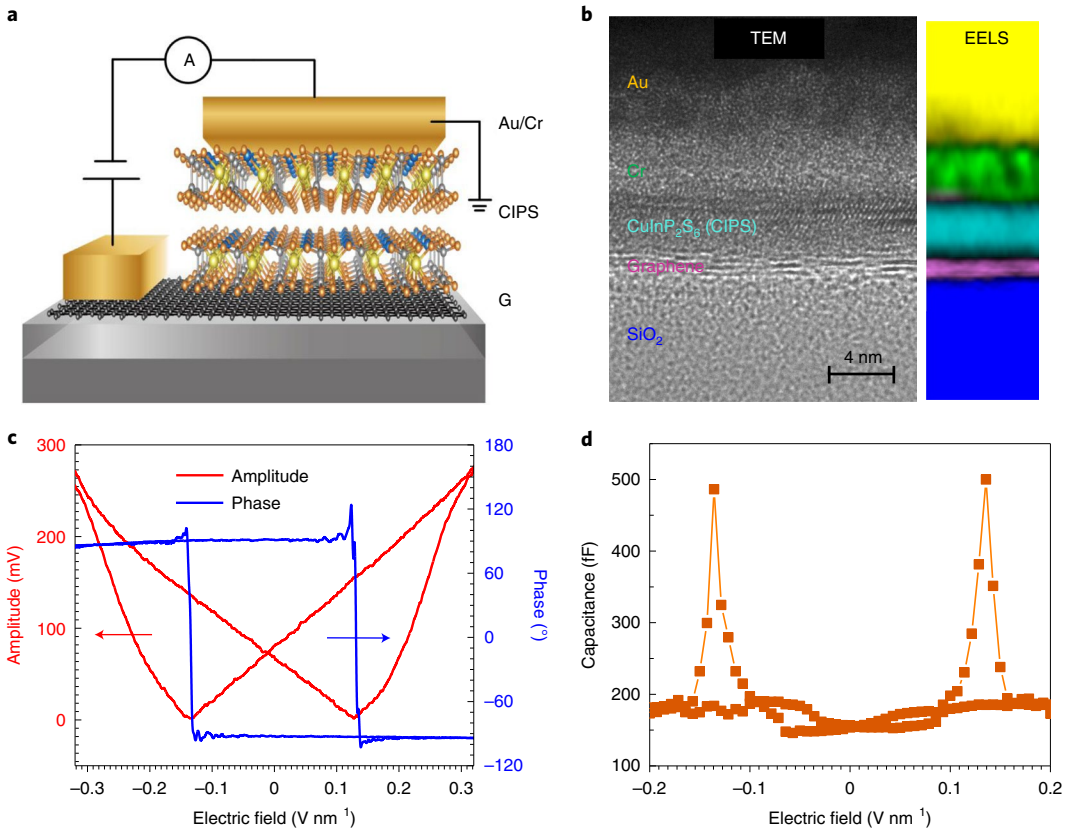

Fig. 1 | The vdW FTJ device structure and the ferroelectric property of CIPS. a, Schematic of the Cr/CIPS/graphene FTJ on the SiO_2/Si substrate. **b**, High-resolution scanning transmission electron microscopy (HRSTEM) and EELS images of a typical vdW FTJ. The layered structure and the material compositions are clearly identified. **c**, Out-of-plane amplitude and phase measurements obtained by PFM on an Au/CIPS/Cr test structure. **d**, Capacitance–electric field characteristics obtained using capacitance–voltage (*C*–*V*) measurement on an Au/CIPS/Cr test structure. The CIPS sample is 20 nm thick in both **c** and **d**. The measurements in **c** and **d** were carried out at ~300 kHz at room temperature.

measurement. The ferroelectricity of the CIPS at room temperature is thus verified. Moreover, by integrating the *C*–*V* characteristics, the remnant polarization (P_r) of this CIPS sample is obtained as ~8 μC cm^{-2}.

The electrical characteristics of a typical Cr/CIPS/graphene vdW FTJ is shown in Fig. 2 for a device with a 4-nm-thick CIPS layer and a 1LG bottom contact. In Fig. 2a, the corresponding tunnelling resistances of the junction are plotted as a function of the switching voltage pulses applied to change the ferroelectric polarization within the CIPS layer. The hysteresis loops move counterclockwise as a function of the applied voltage pulse train, as illustrated in the inset of Fig. 2a. The blue arrows indicate the resistances measured using a 0.4 V probing voltage as the switching voltage pulses change from 0 V to 4.5 V, 4.5 V to 0 V, 0 V to −5.5 V and finally back to 0 V. The switching voltages (4 nm CIPS) are consistent with the PFM measurement performed at the same frequency (Supplementary Fig. 3). Figure 2b shows the *I*–*V* characteristics of the device. The high- and low-resistance states are separately set by voltage pulses of 4.5 V and −5.5 V, respectively, to obtain the corresponding *I*–*V* characteristics. A large TER above 10^7 is obtained in this Cr/CIPS/graphene structure at a bias voltage ~1 V. When obtaining the *I*–*V* characteristics of each state, the voltage sweeps within a relatively small range (from −1 to 1 V) to avoid flipping the direction of the ferroelectric polarization in the CIPS during the measurement. The tunnelling current is low (~10^{-12} A) in the off state and sufficiently high (10^{-5} A) during the on state in this heterostructure, with a TER above 10^7. This is at least an order of magnitude above the TER (10^6) previously reported in ABO-type perovskite FTJs[12].

Origin of the ultra-high TER

To understand the results, quantum transport simulations based on the non-equilibrium Green's function (NEGF) formalism, as described in detail in Supplementary Note 1, were performed to calculate the *I*–*V* characteristics, as shown by the dashed lines in Fig. 2b. The device simulation results indicate that the large TER ratio can be attributed to the efficient modulation of the Fermi level in the graphene contact by the ferroelectric polarization field, and the large effective mass in the vertical direction of the vdW CIPS layer. In contrast to a metal or heavily doped semiconductor contact, a 1LG contact has a low quantum capacitance near its Dirac point, which results in highly efficient modulation of the contact barrier height. By using a graphene contact and a metal contact in the FTJ, as shown in Fig. 1a, asymmetry of the two contact interfaces can lead to a large modulation of the ABH when the ferroelectric polarization switches its direction, which exponentially influences the tunnelling current. Band diagrams of the on and off states are shown schematically in Fig. 3a (also see Supplementary Note 2). The built-in polarization electric field within the CIPS tunnelling barrier layer induces charges at both interfaces between the CIPS layer and the Cr and graphene electrodes. For the on state, the induced charges on the graphene side dopes graphene from relatively intrinsic to n-type and causes the Fermi level to shift from relatively intrinsic to well above the Dirac point, as shown on the left side of Fig. 3a. The increasing Fermi level decreases the ABH, resulting in higher probability for the electrons to tunnel through the CIPS, and hence induces larger tunnelling current. On the other hand, during the off state, the ferroelectric polarization field in the

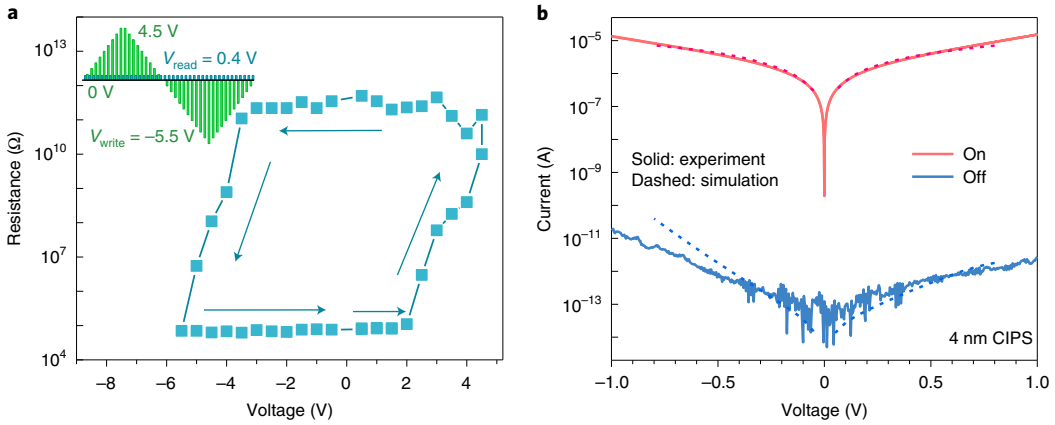

Fig. 2 | Electrical characteristics of the vdW FTJ. a, Resistance versus pulse-voltage loop measured by applying the voltage pulse train (shown in the inset). **b**, Current–voltage characteristics of the vdW FTJ with 4 nm CIPS and 1LG contact, showing TER above 10^7 between the on and off states. The dashed lines show the non-equilibrium Green's function (NEGF) simulation results of the device characteristics, which are consistent with the experimental measurements.

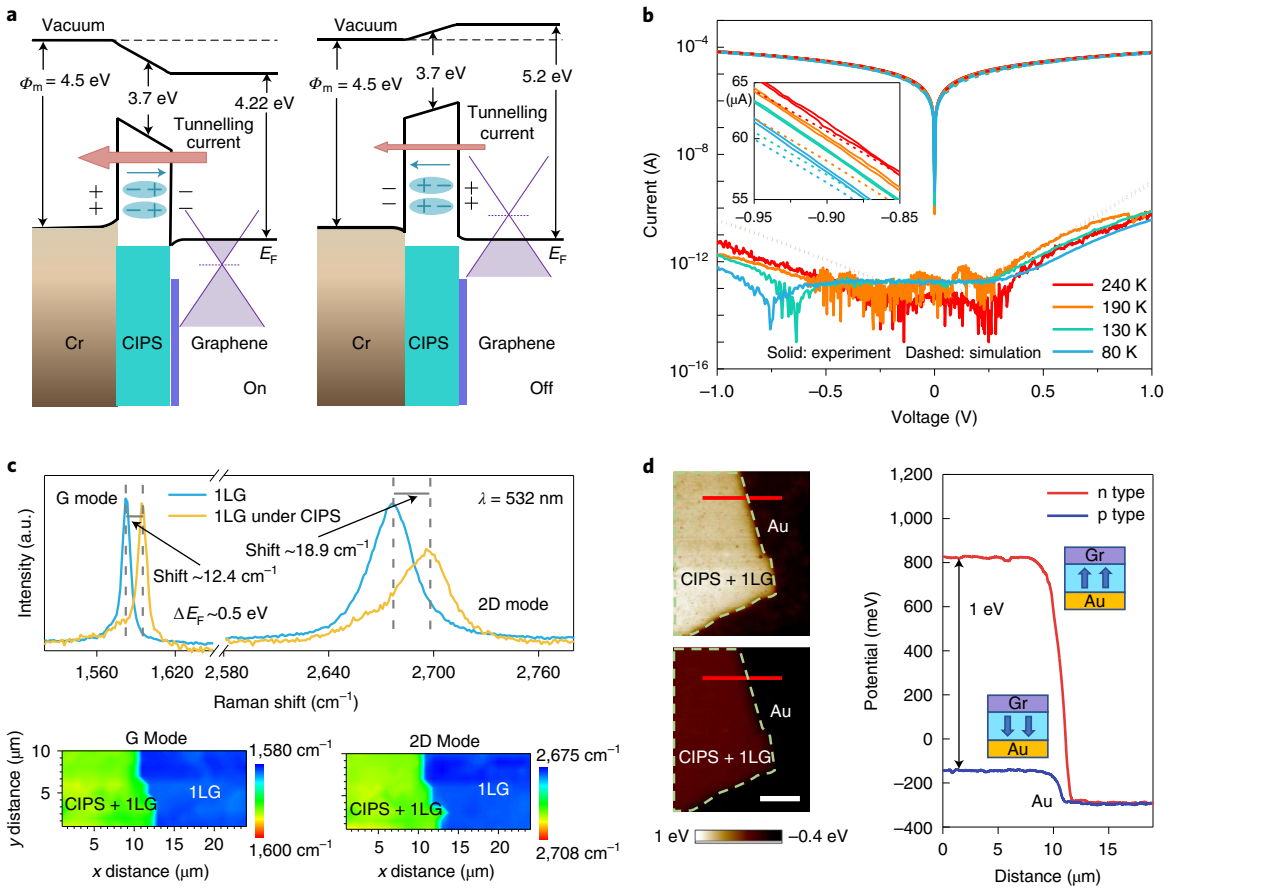

Fig. 3 | Origin of the giant TER. a, Band diagrams for the on and off states of the vdW FTJ operation. The built-in polarization field in the CIPS is shown with cyan arrows, and the tunnelling current is indicated by pink arrows. The work function Φ_m (or electron affinity) of each material is also indicated. **b**, *I*–*V* characteristics of both the on and off states at temperatures of 240, 190, 130 and 80 K. The experimental data are shown as solid lines and the NEGF simulation results are shown as dashed lines. The on-state currents at the four different temperatures are shown in a linear scale in the inset. **c**, Top panel: Raman spectra of bare 1LG (blue) and 1LG under CIPS (yellow) in the wavelength range of the G and 2D modes under excitation with 532-nm light. The shifts in the Raman peaks and the corresponding Fermi level shift (ΔE_f) are indicated. Dashed lines are guides to the eye. Bottom panels: Corresponding Raman frequency mappings showing the shift in the G (left) and 2D (right) modes of the 1LG and nearby 1LG + CIPS. **d**, Left: Surface potential images of the 1LG stacked on top of CIPS/Au after the ferroelectric polarization in the CIPS layer is set to be pointing upwards (n-type doping in graphene, top) and downwards (p-type doping in graphene, bottom). Scale bar, 10 μm. Right: Line plots of the surface potential along the corresponding cuts in the images in the left panels.

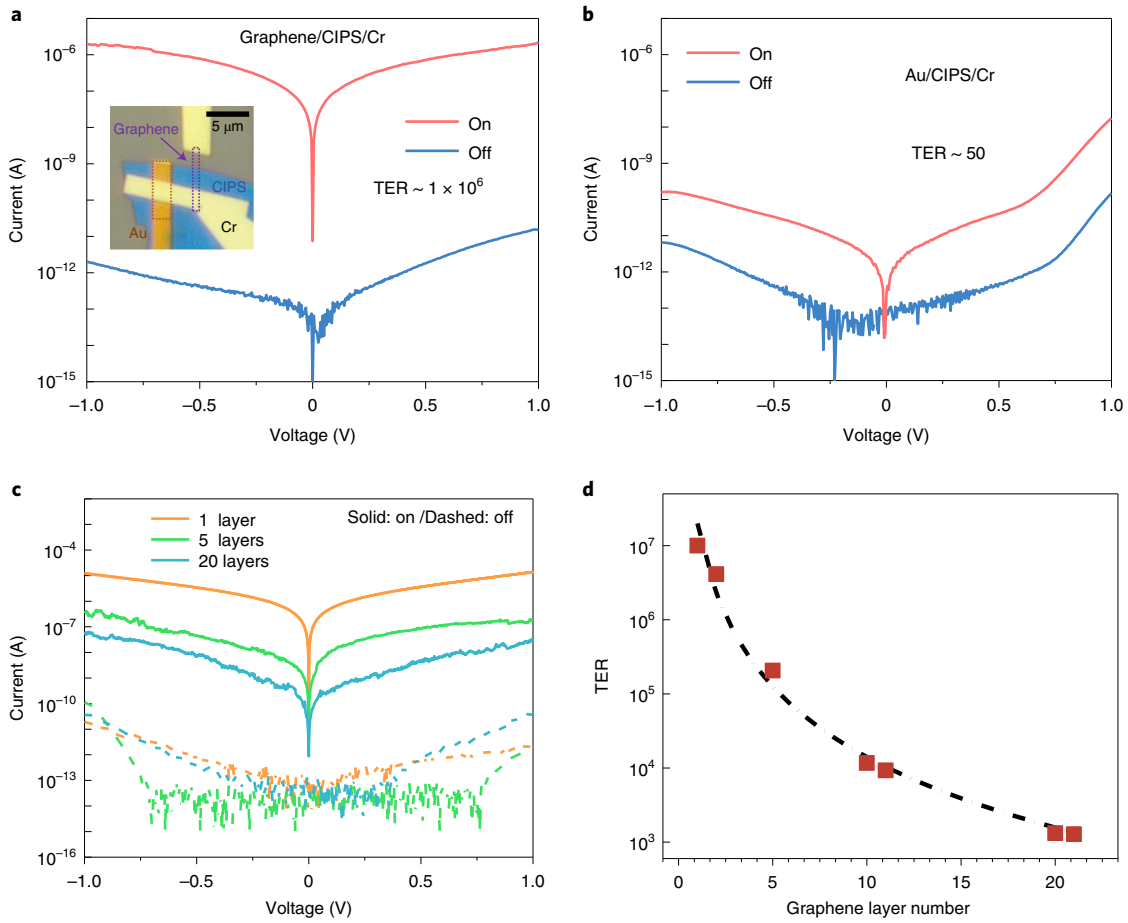

Fig. 4 | Effect of the graphene semi-metallic contact on the vdW FTJ characteristics. a,**b**, Current–voltage characteristics of the on and off states for bilayer graphene/CIPS/Cr (**a**) and Au/CIPS/Cr FTJ (**b**) heterostructures. These heterostructures were fabricated side by side on the same CIPS sheet. The dashed boxes in the inset in **a** outline the underlying bilayer graphene (purple) and Au (orange) bottom contacts of the two heterostructures. The top electrode is Cr in both devices. **c**, *I*–*V* characteristics of three vdW FTJs with different graphene bottom contact thicknesses. **d**, Dependence of the TER on the thickness (in terms of the number of graphene atomic layers) of the graphene bottom contact. The dash-dotted line is a guide to the eye.

CIPS layer is switched to the opposite direction, which induces positive charges on the graphene and dopes the graphene bottom contact to p-type. Thus, the Fermi level in graphene during the off state decreases from the intrinsic to well below the Dirac point, leading to a significant increase in the ABH, as shown on the right side of Fig. 3a. It therefore becomes more difficult for electrons to tunnel through the junction and leads to an ultra-low off-state current (~10^{-12} A). Based on the Raman and surface potential measurement (discussed later), the shift in the graphene Fermi level between the on and off states can be as large as 1 eV, leading to the high TER.

Furthermore, a large effective mass in the vertical direction of the layered CIPS material due to weak vdW bonding can increase the TER ratio exponentially (Supplementary Note 1). Indeed, according to first-principles calculations, the out-of-plane effective mass of CIPS (~$1.3m_0$, where m_0 is the free electron mass) is about three times of that in the in-plane crystal direction (Supplementary Fig. 4), which is similar to the case in other vdW layered materials, such as black phosphorus[37] and MoS_2 (ref. [38]). The unique properties of both the 2D graphene and CIPS materials are thus crucial for achieving the high TER ratio.

There are three possible transport mechanisms in ultra-thin FTJs: Fowler–Nordheim (FN) tunnelling, direct tunnelling and thermionic emission[1]. The FN tunnelling usually dominates at large voltage[7], which is not observed here in Figs. 2 and 3. To verify that the carrier transport mechanism is dominated by direct tunnelling instead of thermionic emission, temperature-dependent *I*–*V* measurements were performed, as shown in Fig. 3b. For both the on and off states, the *I*–*V* characteristics show very weak variations within a large temperature range (from 80 to 240 K). The NEGF simulation results, as shown by the dashed lines in Fig. 3b, also indicate weak temperature dependence, in agreement with the experimental data. This confirms that the dominant transport mechanism here is direct tunnelling, because, as a thermally activated process, the thermionic emission mechanism would have led to a strong temperature dependence in the *I*–*V* characteristics[1].

Giant modulation of the barrier height

The Fermi-level shift in the graphene contact was first verified using Raman spectroscopy measurements. As shown in Fig. 3c, the G and 2D modes of the 1LG under the CIPS both have blueshifts of more than 12 cm^{-1} compared to the 1LG region alone. These shifts are attributed to the changes in the doping level of the 1LG[39–42] due to the effect of the ferroelectric polarization field in the CIPS layer acting on the graphene sheet. Another possible external perturbation that could have led to such large blueshift of both the G and 2D modes in 1LG is the compression strain[39], which was precluded in this heterostructure through thermal annealing before the measurements to relax the strain[43]. Moreover, the shift in the Fermi level (ΔE_f) of the 1LG can be quantitatively given as $|\Delta E_f| \approx \Delta\omega(\mathrm{G})/21 \approx 0.5$ eV, where $\Delta\omega$(G) is the shift in the G-mode peak[39–41]. As well as the blueshifts

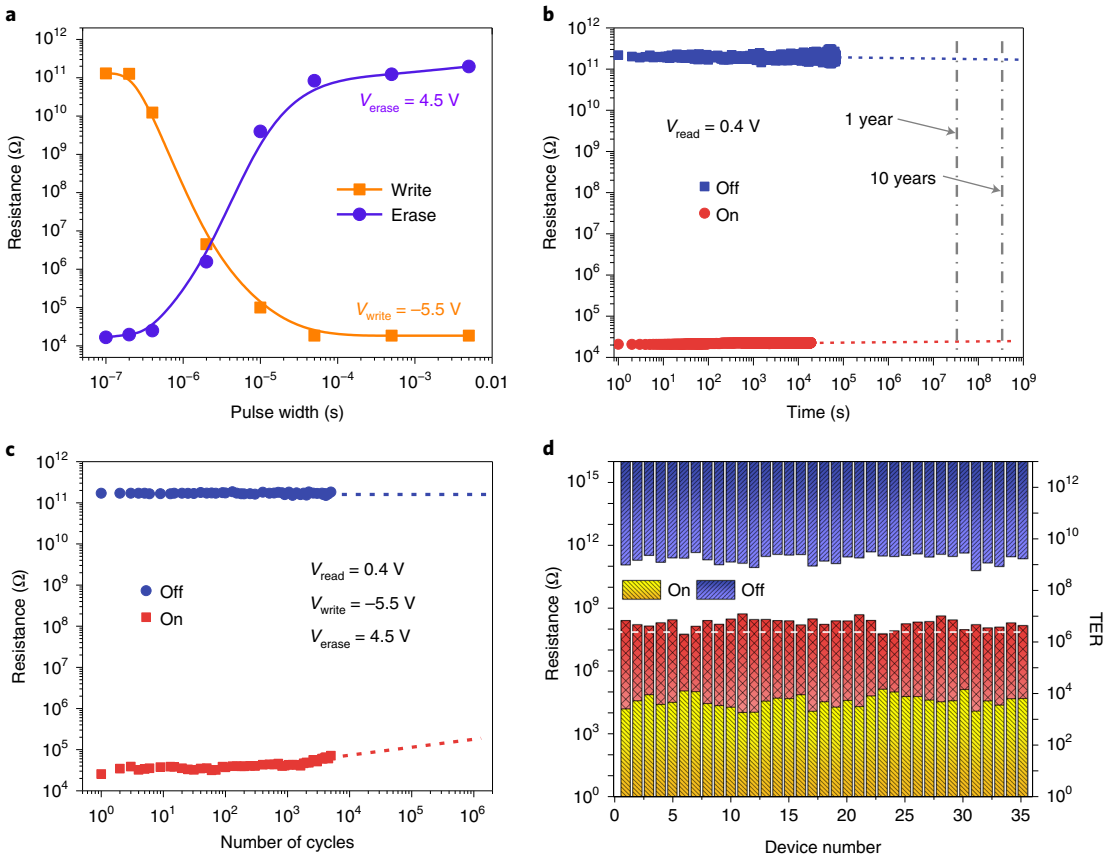

Fig. 5 | Performance of the vdW FTJ as a memory device. a, Switch times of the FTJ from the off state to the on state (write, orange line and squares) and from the on state to the off state (erase, purple line and dots). The write voltage is −5.5 V and the erase voltage is 4.5 V. **b**, Data retention characteristics of the on (red circles) and off (blue squares) states. Dashed lines show the extrapolation of the data retention performance based on the experimental results; 1-year and 10-year marks are indicated on the time axis. **c**, The endurance characteristic of the device. Experimental measurements were obtained for 5,000 switching cycles. Dashed lines show extrapolation up to one million cycles. **d**, The measured on-state (yellow bars) and off-state (blue bars) resistances and the TER (red bars) for 35 FTJ devices from a 5 × 7 array.

in the G and 2D modes, the shift of the Fermi level would result in a decrease in the intensity ratio between the 2D and G modes (I_{2D}/I_G), which is also observed in our measurements, further verifying the doping effect[39,41,42]. This high doping level is primarily due to the built-in electric field in the CIPS layer acting on the 1LG, rather than from charge transfer between the 1LG and CIPS, which, even if present, can only cause a very small doping effect in 2D heterostructures[44]. Because the Raman peak shift resulting from the doping effects does not distinguish between electron or hole doping, this ΔE_f can be either positive or negative depending on whether the Fermi level shifts above or below the Dirac point[41]. Thus, the Fermi level difference for 1LG between the on and off states, based on this estimation, is $2|\Delta E_f| \approx 1$ eV.

To further directly characterize the Fermi-level shift in graphene due to the polarization field switching in CIPS, Kelvin probe force microscopy (KPFM) measurements were used to probe the change in the surface potential, that is, the change in the Fermi level, of the 1LG stacked on the CIPS ferroelectric layer as the polarization in the CIPS layer reverses direction (Fig. 3d). The polarization in the CIPS layer was deterministically switched by the conductive tip of an atomic force microscopy (AFM) system to change the doping type in the 1LG, which in this case was located on top of the CIPS layer (see Methods). The surface potential of the p-doped 1LG was ~0.1 eV higher than that of the gold reference substrate, and the surface potential of the n-doped 1LG was ~1.1 eV higher than that of the gold reference substrate. This shows that the change in the Fermi level in the 1LG is ~1 eV due to switching of the ferroelectric polarization in CIPS, consistent with the values extracted from the Raman spectroscopy measurements. This large Fermi-level shift (~1 eV) is a result of the small density of states and low quantum capacitance in graphene near the Dirac point. Furthermore, numerical simulations of the FTJ device using the NEGF formalism with the effective mass approximation indicate that the P_r of 8 μC cm^{-2} is sufficient for a Fermi-level shift of 1 eV (Supplementary Note 3). The better coupling observed here compared to ABO-type ferroelectrics coupled with graphene[45,46] is reasonable due to the all-vdW nature of the graphene/CIPS interface, which is expected to have minimal dangling bonds, surface reconstruction and defect-mediated interfacial charges.

To further verify the effect of the Fermi-level shift in graphene on the TER, we fabricated both thin graphene (bilayer) and metal (Au) bottom contacts, side by side, under the same CIPS sample (thickness of ~4 nm). The two test structures also share a common top metal electrode (Cr), as shown in the inset of Fig. 4a. The *I*–*V* characteristics of the graphene/CIPS/Cr ferroelectric heterostructure is shown in Fig. 4a and that of the Au/CIPS/Cr heterostructure in Fig. 4b. The off-state tunnelling currents in both structures are at similar levels in the picoampere regime. However, for the on-state current, the structure with the graphene contact is at the μA level, that is, about four orders of magnitude higher than that in the CIPS structure with metal contacts on both sides. The on-state current of the latter structure is at the nA level. This results in a higher TER

($\sim 10^6$) in the graphene-contacted structure (Fig. 4a) compared to the much lower TER (~50) in the structure with metal contacts on both sides (Fig. 4b). Figure 4c,d shows the dependence of the TER on the graphene contact thickness. As the thickness of the graphene bottom contact is increased from a monolayer up to 21 layers in the vdW FTJs (see Supplementary Fig. 5 for AFM measurements of the sample thicknesses) while keeping the CIPS thickness almost constant (~4 nm), the TER decreases as a result of the increasing screening effect leading to a smaller Fermi-level shift with respect to the increasing graphene contact thickness. This also confirms that the high TER is due to the large Fermi-level shift in the 1LG contact.

Switching time, endurance and data retention

Figure 5a shows the resistance of a typical 1LG/CIPS/Cr vdW FTJ as a function of the switching pulse width for both the write (off to on state) and erase (on to off state) operations. The write and erase voltages used are −5.5 V and 4.5 V, respectively. Both the write and erase times are in the range of 10–50 µs, similar to the times for other FTJs reported in the literature with comparable device size[47,48]. The measured switching time is limited by the parasitics in the device due to the relatively large probe contact pads and device size (2 µm × 2 µm). There is significant potential for further improving the switching speed of these devices by removing the probe contact pads and scaling down the device dimensions. Figure 5b characterizes the data retention of this CIPS vdW FTJ, measured at room temperature. The resistance values of the device were measured by first setting the device to the on (off) state and then reading with 0.4 V bias. The TER of the device remained well above 10^7 after more than 8 h, showing robust performance. Figure 5b also shows the extrapolation of the data retention based on the experimental results; 1-year and 10-year marks are indicated on the time axis, revealing the great potential of the device for achieving long data retention time. Figure 5c shows the endurance measurement on this vdW FTJ over 5,000 cycles. Within each cycle, the FTJ is set to the on state by a −5.5 V pulse (10 ms) and read at a bias of 0.4 V, then set to the off state using a 4.5 V pulse (10 ms) and read at a bias of 0.4 V. The TER remains well above 10^6 after 5,000 cycles. Extrapolation based on the experimental data indicates that that the TER can potentially remain above 10^6 after one million switching cycles. To characterize the device uniformity and potential scalability, a 5 × 7 vdW FTJ array was fabricated with graphene contacts (see Supplementary Fig. 6 for the array image). The resistances of the on and off states of these 35 FTJs and the corresponding TERs are shown in Fig. 5d, showing good device uniformity.

Conclusions

We have reported FTJs based on a graphene/CIPS/Cr vdW heterostructure that offer a high TER of above 10^7. Unlike FTJs based on ABO-type perovskites, where the highest TER is enhanced by the modulation of the tunnelling barrier width, our device relies on the large modulation of the tunnelling barrier height. Reversal of the ferroelectric polarization field in CIPS causes a Fermi-level shift of ~1 eV in the graphene contact. The TER is further enhanced by the high carrier effective mass along the out-of-plane crystal direction of the CIPS, and the 4 nm tunnelling barrier is favourable for low-power device operation. Our semimetal–ferroelectric vdW structure provides a new approach for achieving high giant barrier height modulation in FTJ devices, which is a critical step towards developing high-performance ferroelectric and multiferroic materials for memory and computing applications.

Methods

Synthesis of $CuInP_2S_6$ crystals. The $CuInP_2S_6$ (CIPS) crystals were synthesized using a chemical vapour transport method. Powders of Cu, In, P and S were mixed in stoichiometric proportions (mole ratio of Cu:In:P:S = 1:1:2:6, 1 g in total) and flame-sealed in quartz ampoules under vacuum (10^{-4} torr). The ampoules were loaded into a two-zone furnace and heated to ~750–680 °C over a period of 12 h with one end of the ampoules enclosing the powders being placed in the 750 °C zone. The reaction was held at ~750–680 °C for a week and then cooled to room temperature in 24 h. After opening the ampoule, orange platelets embedded in a powder bulk were obtained at the other end of the ampoule (located in the 750 °C zone).

Device fabrication. The graphene sheets were mechanically exfoliated on silicon wafers with 285-nm thermally grown SiO_2. The thin CIPS sample (exfoliated onto polydimethylsiloxane) was then transferred onto the graphene sheet on the Si/SiO_2 wafer using a transfer station with micrometre-resolution alignment under an optical microscope[27]. The sample with the graphene/CIPS heterostructure was then soaked in acetone and isopropanol for 30 min each to remove any potential organic residue on the sample surface. Subsequently, the sample was annealed in an Ar/H_2 (20:1) environment at 300 °C to improve the interfacial quality of the heterostructure. Finally, the top electrode was defined using Raith electron-beam lithography (EBL), which was then formed by depositing 5-nm Cr and 40-nm Au using a Kurt J. Lesker metal evaporator.

STEM and EELS measurement. An FEI Titan Themis G2 system was used to obtain HRSTEM images with four detectors and spherical aberration. The sample was pre-treated by coating with chromium and carbon layers, then thinned by a focused-ion beam (FIB, FEI Helios 450S) with an acceleration voltage of 30 kV. To obtain the HRSTEM image, the acceleration voltage was increased to 200 kV during imaging. EELS signals were collected by a Gatan 977 spectrometer, which was integrated within the STEM system.

Electrical characterization. The *I*–*V* and *C*–*V* characteristics were measured using a Keysight B1500A semiconductor device analyser in a Lakeshore probe station. A cryogenic system was used to measure the temperature-dependent *I*–*V* characteristics. *C*–*V* measurements were carried out using a Keysight N1301A module at 300-kHz frequency.

Simulation. The NEGF formalism was used to treat the quantum transport in the CIPS-based FTJ, as described in detail in the Supplementary Information. Transmission coefficients were calculated at different bias voltages with the NEGF approach, and the current was computed with the Landauer–Büttiker formula. To model the electrostatic effect, a capacitance model, as described in detail in the Supplementary Information, was developed to treat the shift in the graphene Fermi energy level due to the graphene charge, ferroelectric polarization charge and metal screening effects.

Raman spectroscopy. A Renishaw inVia Qontor system with a ×100 objective lens, a grating (1,800 grooves mm^{-1}) and a charge-coupled device camera was used to measure the Raman spectra of the 1LG and CIPS sample. The CIPS sample was set to be polarized before the measurement using the conductive module in a Bruker Dimension Icon AFM system. The wavelength of the excitation laser was 532 nm (from a solid laser), giving a resolution of 1.2 cm^{-1} per pixel. To protect the sample, the laser power was kept below 0.1 mW. The integration time was 20 min for each spectrum to obtain a good signal-to-noise ratio.

PFM and KPFM. A Bruker Dimension Icon system was used for PFM and KPFM measurements. A conductive probe (resistivity of 0.01–0.025 Ω cm, SCM-PIT-V2) with an elastic constant of 3 N m^{-1} was used. For PFM measurements, a resonance frequency of ~300 kHz was used. For KPFM measurements, the lift mode was used with a lift height of 50 nm. To measure the surface potential of the 1LG, the Au/CIPS/1LG structure was used. Ferroelectric polarization within the CIPS was deterministically switched using the tip bias (−6 and 6 V, respectively) in the conductive mode before the KPFM measurements. The surface potential was calibrated using a standard Al–Au sample from Bruker.

Data availability

The data that support the plots within this paper and other findings of this study are available from the corresponding author upon reasonable request.

Received: 26 August 2019; Accepted: 9 June 2020;
Published online: 06 July 2020

References

1. Garcia, V. & Bibes, M. Ferroelectric tunnel junctions for information storage and processing. *Nat. Commun.* **5**, 4289 (2014).
2. Garcia, V. et al. Giant tunnel electroresistance for non-destructive readout of ferroelectric states. *Nature* **460**, 81–84 (2009).
3. Pantel, D., Goetze, S., Hesse, D. & Alexe, M. Reversible electrical switching of spin polarization in multiferroic tunnel junctions. *Nat. Mater.* **11**, 289–293 (2012).
4. Chanthbouala, A. et al. Solid-state memories based on ferroelectric tunnel junctions. *Nat. Nanotechnol.* **7**, 101–104 (2012).

5. Garcia, V. et al. Ferroelectric control of spin polarization. *Science* **327**, 1106–1110 (2010).
6. Zhuravlev, M. Y., Sabirianov, R. F., Jaswal, S. & Tsymbal, E. Y. Giant electroresistance in ferroelectric tunnel junctions. *Phys. Rev. Lett.* **94**, 246802 (2005).
7. Pantel, D. & Alexe, M. Electroresistance effects in ferroelectric tunnel barriers. *Phys. Rev. B* **82**, 134105 (2010).
8. Gruverman, A. et al. Tunneling electroresistance effect in ferroelectric tunnel junctions at the nanoscale. *Nano Lett.* **9**, 3539–3543 (2009).
9. Hambe, M. et al. Crossing an interface: ferroelectric control of tunnel currents in magnetic complex oxide heterostructures. *Adv. Funct. Mater.* **20**, 2436–2441 (2010).
10. Hoffmann, M. et al. Stabilizing the ferroelectric phase in doped hafnium oxide. *J. Appl. Phys.* **118**, 072006 (2015).
11. Ambriz-Vargas, F. et al. A complementary metal oxide semiconductor process-compatible ferroelectric tunnel junction. *ACS Appl. Mater. Interfaces* **9**, 13262–13268 (2017).
12. Xi, Z. et al. Giant tunnelling electroresistance in metal/ferroelectric/semiconductor tunnel junctions by engineering the Schottky barrier. *Nat. Commun.* **8**, 15217 (2017).
13. Dong, Z., Cao, X., Wu, T. & Guo, J. Tunneling current in HfO_2 and $Hf_{0.5}Zr_{0.5}O_2$-based ferroelectric tunnel junction. *J. Appl. Phys.* **123**, 094501 (2018).
14. Bang, T. et al. Low-frequency noise characteristics in SONOS flash memory with vertically stacked nanowire FETs. *IEEE Electron Dev. Lett.* **38**, 40–43 (2016).
15. Muller, J. et al. Ferroelectricity in simple binary ZrO_2 and HfO_2. *Nano Lett.* **12**, 4318–4323 (2012).
16. Mueller, S. et al. Incipient ferroelectricity in Al-doped HfO_2 thin films. *Adv. Funct. Mater.* **22**, 2412–2417 (2012).
17. Wen, Z., Li, C., Wu, D., Li, A. & Ming, N. Ferroelectric-field-effect-enhanced electroresistance in metal/ferroelectric/semiconductor tunnel junctions. *Nat. Mater.* **12**, 617–621 (2013).
18. Liu, F. et al. Room-temperature ferroelectricity in $CuInP_2S_6$ ultrathin flakes. *Nat. Commun.* **7**, 12357 (2016).
19. Ding, W. et al. Prediction of intrinsic two-dimensional ferroelectrics in In_2Se_3 and other III_2-VI_3 van der Waals materials. *Nat. Commun.* **8**, 14956 (2017).
20. Fei, R., Kang, W. & Yang, L. Ferroelectricity and phase transitions in monolayer group-IV monochalcogenides. *Phys. Rev. Lett.* **117**, 097601 (2016).
21. Chandrasekaran, A., Mishra, A. & Singh, A. K. Ferroelectricity, antiferroelectricity, and ultrathin 2D electron/hole gas in multifunctional monolayer MXene. *Nano Lett.* **17**, 3290–3296 (2017).
22. Belianinov, A. et al. $CuInP_2S_6$ room temperature layered ferroelectric. *Nano Lett.* **15**, 3808–3814 (2015).
23. You, L. et al. Origin of giant negative piezoelectricity in a layered van der Waals ferroelectric. *Sci. Adv.* **5**, eaav3780 (2019).
24. Zhou, Y. et al. Out-of-plane piezoelectricity and ferroelectricity in layered α-In_2Se_3 nanoflakes. *Nano Lett.* **17**, 5508–5513 (2017).
25. Xue, F. et al. Room-temperature ferroelectricity in hexagonally layered α-In_2Se_3 nanoflakes down to the monolayer limit. *Adv. Funct. Mater.* **28**, 1803738 (2018).
26. Cui, C., Xue, F., Hu, W.-J. & Li, L.-J. Two-dimensional materials with piezoelectric and ferroelectric functionalities. *npj 2D Mater. Appl.* **2**, 18 (2018).
27. Si, M., Liao, P.-Y., Qiu, G., Duan, Y. & Ye, P. D. Ferroelectric field-effect transistors based on MoS_2 and $CuInP_2S_6$ two-dimensional van der Waals heterostructure. *ACS Nano* **12**, 6700–6705 (2018).
28. Wan, S. et al. Nonvolatile ferroelectric memory effect in ultrathin α-In_2Se_3. *Adv. Funct. Mater.* **29**, 1808606 (2019).
29. Wan, S. et al. Room-temperature ferroelectricity and a switchable diode effect in two-dimensional α-In_2Se_3 thin layers. *Nanoscale* **10**, 14885–14892 (2018).
30. Xue, F. et al. Gate-tunable and multidirection-switchable memristive phenomena in a van der Waals ferroelectric. *Adv. Mater.* **31**, e1901300 (2019).
31. Wang, X. et al. Van der Waals negative capacitance transistors. *Nat. Commun.* **10**, 3037 (2019).
32. Kang, K. et al. High-mobility three-atom-thick semiconducting films with wafer-scale homogeneity. *Nature* **520**, 656–660 (2015).
33. Lin, Y.-M. et al. Wafer-scale graphene integrated circuit. *Science* **332**, 1294–1297 (2011).
34. Wang, L. et al. Epitaxial growth of a 100-square-centimetre single-crystal hexagonal boron nitride monolayer on copper. *Nature* **570**, 91–95 (2019).
35. Maisonneuve, V., Evain, M., Payen, C., Cajipe, V. & Molinie, P. Room-temperature crystal structure of the layered phase $Cu^{II}n^{III}P_2S_6$. *J. Alloys Compd.* **218**, 157–164 (1995).
36. Susner, M. A. et al. High-T_c layered ferrielectric crystals by coherent spinodal decomposition. *ACS Nano* **9**, 12365–12373 (2015).
37. Qiao, J., Kong, X., Hu, Z.-X., Yang, F. & Ji, W. High-mobility transport anisotropy and linear dichroism in few-layer black phosphorus. *Nat. Commun.* **5**, 4475 (2014).
38. Sangwan, V. K. & Hersam, M. C. Electronic transport in two-dimensional materials. *Annu. Rev. Phys. Chem.* **69**, 299–325 (2018).
39. Wu, J.-B., Lin, M.-L., Cong, X., Liu, H.-N. & Tan, P.-H. Raman spectroscopy of graphene-based materials and its applications in related devices. *Chem. Soc. Rev.* **47**, 1822–1873 (2018).
40. Chen, C.-F. et al. Controlling inelastic light scattering quantum pathways in graphene. *Nature* **471**, 617–620 (2011).
41. Das, A. et al. Monitoring dopants by Raman scattering in an electrochemically top-gated graphene transistor. *Nat. Nanotechnol.* **3**, 210–215 (2008).
42. Zhao, W., Tan, P. H., Liu, J. & Ferrari, A. C. Intercalation of few-layer graphite flakes with $FeCl_3$: Raman determination of Fermi level, layer by layer decoupling and stability. *J. Am. Chem. Soc.* **133**, 5941–5946 (2011).
43. Li, H. et al. Interfacial interactions in van der Waals heterostructures of MoS_2 and graphene. *ACS Nano* **11**, 11714–11723 (2017).
44. Sun, Y. et al. Band structure engineering of interfacial semiconductors based on atomically thin lead iodide crystals. *Adv. Mater.* **31**, 1806562 (2019).
45. Baeumer, C., Rogers, S. P., Xu, R., Martin, L. W. & Shim, M. Tunable carrier type and density in graphene/$PbZr_{0.2}Ti_{0.8}O_3$ hybrid structures through ferroelectric switching. *Nano Lett.* **13**, 1693–1698 (2013).
46. Baeumer, C. et al. Ferroelectrically driven spatial carrier density modulation in graphene. *Nat. Commun.* **6**, 6136 (2015).
47. Hu, W. J., Wang, Z., Yu, W. & Wu, T. Optically controlled electroresistance and electrically controlled photovoltage in ferroelectric tunnel junctions. *Nat. Commun.* **7**, 10808 (2016).
48. Jiang, J. et al. Flexible ferroelectric element based on van der Waals heteroepitaxy. *Sci. Adv.* **3**, e1700121 (2017).

Acknowledgements

J.W., H.-Y.C. and H.W. acknowledge support from the Army Research Office Young Investigator Program (grant W911NF-18-1-0268) and the National Science Foundation (grant CCF-1618038). N.Y. and J.G. acknowledge support from the National Science Foundation (grants 1618762, 1610387 and 1904580). J.C. and X.L. acknowledge support from the Semiconductor Research Corporation (SRC).

Author contributions

H.W. conceived the project and led the overall research activities. J.W. and H.-Y.C. fabricated the vdW FTJ devices. J.W., H.-Y.C. and X.Y. performed the electrical measurements and data analysis. N.Y. and J.G. led the research in the theoretical modelling. J.C. and X.L. synthesized the materials. J.W. and F.L. characterized the materials and devices. Q.S. contributed to the formulation of the project idea. J.W., H.-Y.C. and H.W. co-wrote the manuscript with input and comments from all the authors.

Competing interests

The authors declare no competing interests.

Additional information

Supplementary information is available for this paper at https://doi.org/10.1038/s41928-020-0441-9.

Correspondence and requests for materials should be addressed to Q.S., J.G. or H.W.

Reprints and permissions information is available at www.nature.com/reprints.

Publisher's note Springer Nature remains neutral with regard to jurisdictional claims in published maps and institutional affiliations.